Meccanica
https://doi.org/10.1007/s11012-020-01224-z

Modeling of brittle fracture in thick plates subjected to transient dynamic loads using a hybrid phase field model

P. Raghu · A. Rajagopal · S. K. Jalan · J. N. Reddy

Received: 27 March 2020 / Accepted: 2 August 2020

Abstract In this work, we propose a hybrid phase field model for the brittle fracture analysis of thick plates subjected to transient dynamic loads. Shear deformation effects which play important role on the behavior of thick plates are captured by using Reddy's third-order shear deformation theory. The proposed model preserves the linearity of the elastic equilibrium equation within the staggered solution approach and ensures the evolution of damage due to the tensile part of the strain energy. The governing equations of motion of the proposed model are derived by seeking the minimization of the free energy functional. These governing equations are solved in a finite element framework using a staggered solution algorithm. The proposed model is compared with the model with no tension–compression split. Both these models show different mechanical response of thick plates. Using numerical examples, the efficiency of the proposed model in predicting the nucleation and propagation of damage in thick plates subjected to transient dynamic loads is presented.

Keywords Phase field · Free energy functional · Order parameter · Hybrid model · Thick plate · TSDT · Transient dynamic loads

1 Introduction

Transient dynamic loads are characterized by being very short in duration with intense pressure spike. Plate structures such as those used in aerospace and automotive industries are often subjected to these loads. Materials when subjected to these loads, experience complex fracture phenomena. Therefore it is important to perform the computational modeling of fracture to study the mechanical response of these structures under such loads. The computational fracture models can be classified as discrete models (sharp crack models) and diffused models. In the discrete models, the crack is modeled as a discontinuity whereas in diffused models, a smooth approximation of crack surface is made thereby avoiding the discontinuity. Because of the discontinuity they possess in discrete models, they often require remeshing algorithms to track the crack propagation. Computational

In honor of Professor J. N.Reddy for his 75th Birthday.

P. Raghu · A. Rajagopal (✉)
Department of Civil Engineering, Indian Institute of Technology Hyderabad, Hyderabad, India
e-mail: rajagopal@iith.ac.in

S. K. Jalan
VSSC, Indian Space Research Organization, Trivandrum, India

J. N. Reddy
J. Mike Walker '66 Department of Mechanical Engineering, Texas A&M University, College Station, TX 77843-3123, USA

Published online: 10 August 2020

discrete fracture model such as extended finite element method [1–3] though were able to model the fracture without remeshing, they fail to describe the nucleation naturally i.e they need an additional criterion to determine the nucleation of fracture. On the other hand, interface finite elements using cohesive zone models [4] work well only with the pre-existing interfaces [5]. It is also observed that the diffused models based on continuum damage mechanics result in spurious mesh dependencies in modeling softening phenomena [6, 7]. Nonlocal and gradient damage models [8–12] proved to overcome this issue. The phase field model which shares many features of the nonlocal damage models not only alleviates the need for sophisticated algorithms for tracing the crack path but also facilitates the prediction of crack nucleation, propagation, branching and merging in three dimensions without the need for ad-hoc criteria. The phase field method has its foundation in variational approach to fracture. Francfort et al. [13] first posed the problem of modeling the brittle fracture in a variational setting where the evolution of fracture can be obtained by minimizing the free energy functional. This model is variational equivalent to the Griffith's linear elastic fracture model [14]. Phase field method developed by Bourdin et al. [15] is the regularized version of discrete model proposed by Francfort et el. [13]. In this model, the discrete (sharp) crack is approximated as a diffused crack. This necessitates the introduction of a field variable known as *phase field* or *order parameter* as the unknown. In doing so, it also introduces the gradient of the phase field variable which entails the use of length scale parameter. The phase field takes the values ranging from 0 to 1 where the value of zero and one correspond to the undamaged and fully damaged state of the material respectively. This regularized model draws the motivation from *Ambrosio–Tortorelli regularization* of the *Mumford–Shah functional* in image segmentation [16]. It is also seen that, in the sense of Γ convergence, the regularized model reduces to sharp crack model when the length scale parameter (l) tends to zero. Since it is a variational approach and the field variable is included in the free energy functional as an unknown, the evolution of damage can be found as part of the solution of the governing partial differential equations. This makes the method numerically amicable to standard finite element method as there is no need of doing remeshing employing sophisticated algorithms to track the crack propagation.

The phase field (PF) model has been the most sought after technique in the recent times for modeling the fracture (see [17–26]). Some of the applications of phase field models include modeling ductile fracture ([22, 27–30]), modeling fracture with finite strains [31–33], fracture modeling in pressure loading environment [34] and modeling conchoidal fracture [35]. Due to the variational approach to the damage modeling, phase field model naturally describes the evolution of damage which deals with the complex crack topologies such as branching and merging without numerical robustness even in three dimensions. Lee et al. [19] and Borden et al. [36] studied the fracture propagation in three-dimensions. Pham et al. [21] developed a 3D finite element model for the phase field model of brittle fracture and validated with the results obtained from the experiments. Kasirajan et al.[37] modeled brittle fracture in quasi brittle materials using natural neighbor Galerkin method. Applications of phase field model for interface fracture model [22, 38–44] and modeling fracture in composites [45–48] are also reported in the literature. The standard phase field model assumes the phase field variable to be isotropic i.e it is directionally independent at a given material point. This limits the use of this model to capture the crack propagation in anisotropic materials such as polymers, organic materials etc. Raina et al. [17] studied the crack propagation in arterial walls by introducing an anisotropic failure criterion. Solmaz et al. [49] developed a phase field formulation by incorporating the anisotropic surface energy to study the crystal growth. Rajagopal et al [50] used a C^1 natural neighbourGalerkin method to solve the four order Cahn-Hilliard phase field equations. Bin et al. [51] proposed a phase field model with strongly anisotropic surface energy which results in fourth order phase field equation in contrast to the standard second order equation. These works rely on defining the anisotropic surface energy by enriching it with higher order gradients of damage variable. Bleyer et al. [47] proposed a new model which accounts for both the elastic anisotropy and the damage anisotropy.

There have been several works reported so far, that deal with the dynamic fracture in plane problems. Karma et al. [52] first provided a phase field model for

modeling mode III dynamic fracture. Hofacker et al. [53] developed a phase field model for dynamic fracture by employing a tension–compression split in the strain energy. This model ensures the degradation of the tensile part of the strain energy only which is physically more appealing. Borden et al. [54] studied the dynamic fracture in two and three dimensions. Here the authors used T-splines which ensure the local adaptive refinement to simulate the fracture in three dimensions. Recently Nguyen et al. [55] developed a phase field regularized cohesive zone model for modeling dynamic brittle fracture. This model is insensitive to the choice of the length scale parameter unlike the standard phase field model. Very limited studies are available on the application of phase field method to model fracture in thick plates subjected to transverse loads. Amiri et al. [56] first studied fracture behavior in thin shells using Kirchhoff–Love shell theory. Kiendl et al. [57] presented a more accurate model for the fracture analysis in thin plates and shells using Kirchhoff–Love shell model. Raghu et al. [58] presented a hybrid phase field model to model the fracture in thick plates. Areias et al. [59] performed finite strain analysis of plates and shells. Recently, Lai et al. [60] developed a phase field model to study the brittle fracture in Euler– Bernoulli beam accounting transverse part-through fracture. In all these models, the load is considered to be static. There are no works reported so far to study fracture in plates under transient dynamic loads using the phase field method. In this work, we aim to develop a new hybrid phase field model to study the damage propagation in plates under transient dynamic loads.

The *classical theories* such as Euler–Bernoulli and Kirhchhoff–Love are more suitable for the analysis of thin structures where shear deformations can be neglected. However in thick plates where shear deformation significantly affects the overall behavior of the plate, one must use more realistic theories such as shear deformation theories to correctly capture the mechanical behavior. The novelty of this work includes proposing a hybrid phase field model for the fracture modeling in thick plates by invoking a higher-order shear deformation theory such as Reddy's TSDT [61], which requires no shear correction factor and represents the transverse shear stresses quadratically through the plate thickness. The standard phase field model as first proposed by Bourdin et al. [15] causes physically unappealing results as this model predicts cracking in pure compression also. To avoid this discrepancy, Amor et al. [62] and Miehe et al. [63] modified the Bourdin's phase field model by introducing the decomposition of the strain energy into the formulation. In these models, the degradation is applied only on the tensile part of strain energy in defining the stress. However, this split makes the elastic equilibrium equation nonlinear which increases the computational cost. The proposed phase field model not only retains the linearity of the elastic equilibrium equation within the staggered approach and also ensures the evolution of damage caused only by the tensile part of strain energy. More details on this model are presented in Sect. 3.1.

The outline of the paper is as follows. In Sect. 2, we present both the sharp and phase field crack topologies and the regularized crack functional. In Sect. 3, we present the proposed hybrid phase field formulation for the transient dynamic analysis. Finite element model of the governing equations are also presented in this section. In Sect. 4, we present the implementation aspects. Sect. 5 presents different numerical examples to show the effectiveness of the present model. Finally Sect. 6 presents the conclusions drawn from the work.

2 Phase-field description of fracture

In this section, we introduce the phase field method in the context of fracture modeling. PF method serves an approximation to the discrete fracture models in the sense that the sharp crack surface is approximated by a diffused crack surface. As shown in Fig. 1, a sharp crack topology is approximated as a diffused crack spread over region of radius equal to twice the length scale parameter l. The variable introduced here ensures the smooth transition between undamaged and fully damaged material. The range of phase field varies from 0 to 1 with the value *zero* corresponds to the undamaged material and the value *one* corresponds to the fully damaged material.

The regularized crack surface functional can be written as (see 15, 64),

$$\Gamma_l = \int_\Omega \gamma(\phi, \nabla\phi)\, dV \tag{1}$$

where, γ is the crack surface density, which can be expressed in terms of crack phase field (ϕ) and its

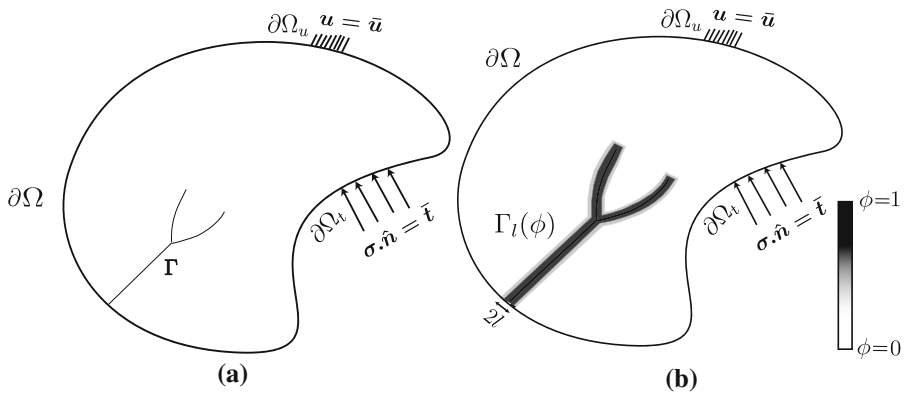

Fig. 1 2D representation of **a** sharp crack topology and **b** phase field crack topology

gradient with in the localization region ($dV = \Gamma dz$, Γ is the crack surface) as

$$\gamma(\phi, \nabla\phi) = \frac{\phi^2}{2l} + \frac{l}{2}|\nabla\phi|^2 \tag{2}$$

3 Formulation

Following the regularized variational fracture model of Bourdin et al. [15], the free energy functional for plate structures with a regularized crack surface density can be written as,

$$E_l = \int_\Omega \Big(g(\phi)\psi_{es} - \psi_{ek}\Big)\, dV + \int_\Omega \psi_\phi\, dV \tag{3}$$

where

$$\begin{aligned} &\int \psi_\phi(\phi, \nabla\phi)\, dV = \int_A \int_{-\frac{h}{2}}^{\frac{h}{2}} \psi_\phi\, dA\; dz \\ &= \int_A hG_c\Big\{\frac{\phi^2}{2l} + \frac{l}{2}|\nabla\phi|^2\Big\}\, dA \end{aligned} \tag{4}$$

where ψ_{es} and ψ_{ek} represent the elastic strain energy density and the kinetic energy density respectively and A represents the surface area of the midplane of the plate. The damage parameter ϕ is assumed to be uniform through the thickness; h represents the thickness of the plate and G_c represents the Griffith's critical energy density. $g(\phi)$ is called the degradation function which is introduced to ensure the degradation of stiffness as the damage progresses in the bulk material.

The degradation function can be taken as

$$g(\phi) = (1-\eta)(1-\phi)^2 + \eta \tag{5}$$

where η is a very small positive scalar value ($<<1$) introduced to avoid the ill conditioning of the stiffness matrix when $\phi = 1$. As it can be seen the $g(\phi)$ attains the value 1 and $\eta \ll 1$ in the undamaged state and fully damaged state respectively. Thermodynamic conjugate force $F = -g'(\phi)\psi_{es}$ takes the value zero when the material is fully damaged as $g'(1) = 0$.

3.1 Hybrid phase field model of brittle fracture for plates

To avoid the nonlinearity in the elastic equilibrium equation due to tension–compression split of the strain energy, in this section we propose a hybrid phase field model for the analysis of plates under transient dynamic loads.

In the hybrid model, the linearity of the elastic equilibrium equation is preserved (within the staggered approach) as there is no split applied on ψ_{es} in defining the stress. Though the hybrid model possesses variational inconsistency, an alternate approach can be presented to derive the evolution equation as shown in Ambati et al. [26] where the authors proposed this first for the plane problems. The model also does not violate the second law of thermodynamics[65]. To ensure the evolution of damage only due to the tensile part of the strain energy, the history variable based on ψ_{es}^+ is supplied to the phase field evolution equation. Therefore the regularized free energy functional for the analysis of plates can be written as

$$E_l = \int_A \left(g(\phi)\psi_s - \psi_k + hG_c\{\frac{\phi^2}{2l} + \frac{l}{2}|\nabla\phi|^2\}\right) dA \tag{6}$$

where ψ_s and ψ_k are the elastic strain energy density and the kinetic energy obtained after integrating through the thickness.

$$\psi_\alpha = \int_{-\frac{h}{2}}^{\frac{h}{2}} \psi_{e\alpha}(z)\, dz \tag{7}$$

where α takes the symbols s and k. The thickness-wise integration can be done using the Simpson's rule.

3.1.1 Plate kinematics

To capture the shear deformation effects especially in thick plates, Reddy's third order shear deformation theory [61] has been used in this work for deriving the elastic equilibrium equations. The in-plane displacements are expanded up to the third degree of the thickness coordinate hence TSDT predicts the quadratic variation of transverse shear strains through the thickness of the plate. Therefore TSDT does not require a shear correction factor. The deformation of the normal line according to TSDT is shown in Fig. 2.

The total displacement of a point **a** as shown in Fig. 2 can be written as

$$\begin{aligned} u(x,y,z) &= u_0(x,y) + z\phi_x \\ &\quad - \frac{4z^3}{3h^2}\left(\phi_x \right. \\ &\quad \left. + \frac{\partial w_0}{\partial x}\right) \\ v(x,y,z) &= v_0(x,y) + z\phi_y \\ &\quad - \frac{4z^3}{3h^2}\left(\phi_y \right. \\ &\quad \left. + \frac{\partial w_0}{\partial y}\right) \\ w(x,y,z) &= w_0(x,y) \end{aligned} \tag{8}$$

where (u_0, v_0) are in-plane displacements of a point on the mid-plane (i.e., $z = 0$) and w_0 represents the transverse displacement. ϕ_x and ϕ_y represent the rotations of a transverse normal line at the mid-plane ($\phi_x = \frac{\partial u}{\partial z}$ and $\phi_y = \frac{\partial v}{\partial z}$) and h represents the thickness of the plate.

3.1.2 Strain–displacement relations

The strain components for the linear strains of third-order shear deformation theory are

$$\begin{Bmatrix} \varepsilon_{xx} \\ \varepsilon_{yy} \\ \gamma_{xy} \end{Bmatrix} \tag{9}$$

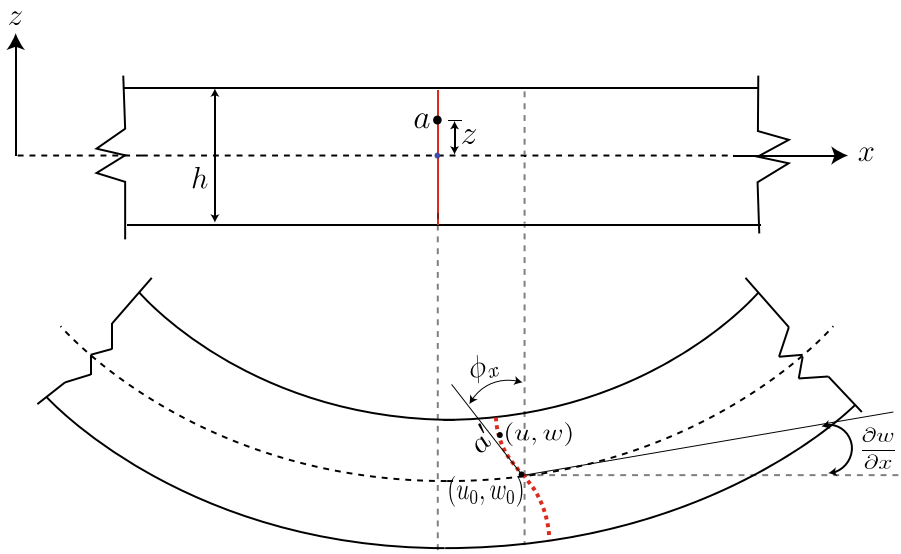

Fig. 2 Undeformed and deformed shape of the plate according to TSDT

$$\begin{Bmatrix} \gamma_{yz} \\ \gamma_{xz} \end{Bmatrix} \tag{10}$$

where

$$\begin{Bmatrix} \varepsilon_{xx}^{(0)} \\ \varepsilon_{yy}^{(0)} \\ \gamma_{xy}^{(0)} \end{Bmatrix} = \begin{Bmatrix} \dfrac{\partial u_0}{\partial x} \\ \dfrac{\partial v_0}{\partial y} \\ \dfrac{\partial u_0}{\partial y} + \dfrac{\partial v_0}{\partial x} \end{Bmatrix}, \begin{Bmatrix} \varepsilon_{xx}^{(1)} \\ \varepsilon_{yy}^{(1)} \\ \gamma_{xy}^{(1)} \end{Bmatrix} = \begin{Bmatrix} \dfrac{\partial \phi_x}{\partial x} \\ \dfrac{\partial \phi_y}{\partial y} \\ \dfrac{\partial \phi_x}{\partial y} + \dfrac{\partial \phi_y}{\partial x} \end{Bmatrix} \tag{11}$$

$$\begin{Bmatrix} \varepsilon_{xx}^{(3)} \\ \varepsilon_{yy}^{(3)} \\ \gamma_{xy}^{(3)} \end{Bmatrix} = -c_1 \begin{Bmatrix} \dfrac{\partial \phi_x}{\partial x} + \dfrac{\partial^2 w_0}{\partial x^2} \\ \dfrac{\partial \phi_y}{\partial y} + \dfrac{\partial^2 w_0}{\partial y^2} \\ \dfrac{\partial \phi_x}{\partial y} + \dfrac{\partial \phi_y}{\partial x} + 2\dfrac{\partial^2 w_0}{\partial x \partial y} \end{Bmatrix} \tag{12}$$

$$\begin{Bmatrix} \gamma_{yz}^{(0)} \\ \gamma_{xz}^{(0)} \end{Bmatrix} = \begin{Bmatrix} \phi_y + \dfrac{\partial w_0}{\partial y} \\ \phi_x + \dfrac{\partial w_0}{\partial x} \end{Bmatrix}, \begin{Bmatrix} \gamma_{yz}^{(2)} \\ \gamma_{xz}^{(2)} \end{Bmatrix} = -c_2 \begin{Bmatrix} \phi_y + \dfrac{\partial w_0}{\partial y} \\ \phi_x + \dfrac{\partial w_0}{\partial x} \end{Bmatrix} \tag{13}$$

$c_2 = 3c_1$, $c_1 = \frac{4}{3h^2}$. As it can be seen in Eq. (10), the transverse shear strains vary quadratically through the thickness of the plate.

3.1.3 Governing equations

The expressions for the strain energy and the kinetic energy can be written as

$$\int \psi_{es}\, dV = \frac{1}{2}\int_A \int_{-\frac{h}{2}}^{\frac{h}{2}} \left(\sigma_{xx}\varepsilon_{xx} + \sigma_{yy}\varepsilon_{yy} + \sigma_{xy}\gamma_{xy} + \sigma_{xz}\gamma_{xz} + \sigma_{yz}\gamma_{yz}\right) dA\, dz \tag{14}$$

$$\int \psi_{ek}\, dV = \frac{1}{2}\int_A \int_{-\frac{h}{2}}^{\frac{h}{2}} \rho\left(\dot{u}^2 + \dot{v}^2 + \dot{w}^2\right) dA\, dz \tag{15}$$

where $\dot{u}, \dot{v}, \dot{w}$ represent the time derivatives of u, v, w respectively.

The governing equations can be obtained by invoking the Euler equation. For a given functional I and Lagrangian L of the form,

$$I = \int_\Omega L(\alpha, \nabla\alpha)\, d\Omega \tag{16}$$

the Euler equation is written as,

$$\frac{\delta I}{\delta \alpha} = \frac{\partial L}{\partial \alpha} - \nabla \cdot \frac{\partial L}{\partial \nabla \alpha} = 0 \tag{17}$$

The Euler equation leads to the following two sets of governing equations

$$\frac{\partial N_{xx}}{\partial \mathrm{x}} + \frac{\partial N_{xy}}{\partial \mathrm{y}} = I_0\ddot{u}_0 + J_1\ddot{\phi}_x - c_1 I_3 \frac{\partial \ddot{w}_0}{\partial x} \tag{18a}$$

$$\frac{\partial N_{xy}}{\partial \mathrm{x}} + \frac{\partial N_{yy}}{\partial \mathrm{y}} = I_0\ddot{v}_0 + J_1\ddot{\phi}_y - c_1 I_3 \frac{\partial \ddot{w}_0}{\partial y} \tag{18b}$$

$$\begin{aligned} &\frac{\partial \bar{Q}_x}{\partial \mathrm{x}} + \frac{\partial \bar{Q}_y}{\partial \mathrm{y}} + c_1\left(\frac{\partial^2 P_{xx}}{\partial \mathrm{x}^2} + 2\frac{\partial^2 P_{xy}}{\partial \mathrm{x}\,\partial \mathrm{y}} + \frac{\partial^2 P_{yy}}{\partial \mathrm{y}^2}\right) + q \\ &\quad = I_0\ddot{w}_0 - c_1^2 I_6\left(\frac{\partial^2 \ddot{w}_0}{\partial x^2} + \frac{\partial^2 \ddot{w}_0}{\partial y^2}\right) \\ &\quad + c_1\left[I_3\left(\frac{\partial \ddot{u}_0}{\partial x} + \frac{\partial \ddot{v}_0}{\partial y}\right) + J_4\left(\frac{\partial \ddot{\phi}_x}{\partial x} + \frac{\partial \ddot{\phi}_y}{\partial y}\right)\right] \end{aligned} \tag{18c}$$

$$\frac{\partial \bar{M}_{xx}}{\partial \mathrm{x}} + \frac{\partial \bar{M}_{xy}}{\partial \mathrm{y}} - \bar{Q}_x = J_1\ddot{u}_0 + K_2\ddot{\phi}_x - c_1 J_4 \frac{\partial \ddot{w}_0}{\partial x} \tag{18d}$$

$$\frac{\partial \bar{M}_{xy}}{\partial \mathrm{x}} + \frac{\partial \bar{M}_{yy}}{\partial \mathrm{y}} - \bar{Q}_y = J_1\ddot{v}_0 + K_2\ddot{\phi}_y - c_1 J_4 \frac{\partial \ddot{w}_0}{\partial y} \tag{18e}$$

and

$$\frac{hG_c}{\bar{d}}\left(\phi - l^2\nabla \cdot \nabla\phi\right) = 2(1-\eta)(1-\phi)\mathcal{H}^+ \tag{19}$$

where the in-plane force resultants ($N_{\alpha\beta}$), moment resultants ($M_{\alpha\beta}$), higher order stress resultants ($P_{\alpha\beta}$) and the transverse force resultants (Q_α, R_α) are given by

$$\begin{aligned} \begin{Bmatrix} N_{\alpha\beta} \\ M_{\alpha\beta} \\ P_{\alpha\beta} \end{Bmatrix} &= \int_{-\frac{h}{2}}^{\frac{h}{2}} g(\phi)\sigma_{\alpha\beta} \begin{Bmatrix} 1 \\ z \\ z^3 \end{Bmatrix} dz, \quad \begin{Bmatrix} Q_\alpha \\ R_\alpha \end{Bmatrix} \\ &= \int_{-\frac{h}{2}}^{\frac{h}{2}} g(\phi)\sigma_{\alpha z} \begin{Bmatrix} 1 \\ z^2 \end{Bmatrix} dz \end{aligned} \tag{20}$$

with $c_1 = \frac{4}{3h^2}, c_2 = 3c_1, \quad \bar{M}_{\alpha\beta} = M_{\alpha\beta} -$

$c_1 P_{\alpha\beta}$, and $\bar{Q}_\alpha = Q_\alpha - c_2 R_\alpha$ and the mass moments of inertia are given by

$$I_i = \int_{\frac{-h}{2}}^{\frac{h}{2}} \rho(z)^i dz \, (i = 0, 1, 2, 3, 4, 6),$$
$$K_2 = I_2 - 2c_1 I_4 + c_1^2 I_6 \quad \text{and} \quad J_i = I_i - c_1 I_{i+2}, \ (i = 1, 4) \tag{21}$$

α, β take the symbols x and y and $\mathcal{H}^+_{t \in [0,\tau]} = \max \psi_s^+(\boldsymbol{\varepsilon}, t)$. It ensures the crack irreversibility and facilitates the decoupling of two sets of governing equations.

The positive energy calculation is done as follows

$$\psi_{es}^+ = \frac{1}{2}\lambda\left(\langle tr(\boldsymbol{\varepsilon})\rangle^+\right)^2 + \mu tr\left(\boldsymbol{\varepsilon}^+\right)^2 - \frac{\lambda^2}{2(\lambda + 2\mu)}\left(\langle tr(\boldsymbol{\varepsilon})\rangle^+\right)^2 + \frac{1}{2}\mu(\gamma_{xz}^2 + \gamma_{yz}^2) \tag{22}$$

The above formula draws the motivation from the work of Kiendl et al. [57] where the authors derived it for the Kirchhoff–Love plate theory. The above split is based on the spectral decomposition of the strain tensor; $\boldsymbol{\varepsilon} = \sum_{i=1}^3 \langle \varepsilon_i \rangle \boldsymbol{n_i} \otimes \boldsymbol{n_i}$, $\boldsymbol{\varepsilon}_\pm = \sum_{i=1}^3 \langle \varepsilon_i \rangle_\pm \boldsymbol{n_i} \otimes \boldsymbol{n_i}$ where ε_i and $\boldsymbol{n_i}$ are the principal strains and their directions respectively, λ, μ are Lamé parameters and $\langle \alpha \rangle_\pm = \frac{1}{2}(\alpha \pm |\alpha|)$.

3.1.4 Finite element model

Finite element model of Eq. (19) is developed in this section. We refer to the works of Raghu et al. [66, 67] for the discretized weak form of the Eq. (18). The weak forms for the evolution Eq. (19) can be obtained as follows:

$$\int_A \delta w \left(\frac{hG_c}{l}(\phi - l^2 \triangle \phi) - 2(1-\eta)(1-\phi)\mathcal{H}^+\right) dA = 0 \tag{23}$$

where δw is the weighting function. The use of divergence theorem further leads to the following

$$\int_A \left\{\delta w \frac{hG_c}{l}\phi + hG_c l \nabla\phi \cdot \nabla \delta w - 2(1-\eta)(1-\phi)\mathcal{H}^+ \delta w\right\} dA - \oint_{\partial A} hG_c l \partial w \nabla \phi \cdot \hat{} dS = 0 \tag{24}$$

where $\hat{}$ represents the unit outward normal vector.

3.1.5 Finite element approximation

The primary variable ϕ can be approximated using Lagrangian interpolation functions in a given finite element as:

$$\phi = \sum_{j=1}^{n} \phi_j N_j \tag{25}$$

where N_j are the Lagrange interpolation functions and n is the total number of degree of freedom in a given element. Substitution of this approximation in the weak form i.e Eq. (24), leads to the following discretized form of the weak form

$$[\boldsymbol{K}]\{\phi\} = \boldsymbol{f} \tag{26}$$

The stiffness matrix and force vector are given as

$$K_{ij}^{\phi\phi} = \int_A \left\{\frac{hG_c}{l} N_i N_j + hG_c l\left(\frac{\partial N_i}{\partial x}\frac{\partial N_j}{\partial x} + \frac{\partial N_i}{\partial y}\frac{\partial N_j}{\partial y}\right) + 2(1-\eta)\mathcal{H}^+ N_i N_j\right\} dxdy \tag{27}$$

$$f_i^\phi = \int_A 2(1-\eta)\mathcal{H}^+ N_i \, dx \, dy \tag{28}$$

The discretized weak form of the elastic equilibrium equation (see [66] and [68] for more details) using TSDT suggests that the finite element should possess 8 no. of degree of freedom at each node. These dof's are approximated in the following manner:

$$u(x, y, t) \approx \sum_{j=1}^{m} U_j(t) N_j^{(1)}(x, y) \tag{29}$$

$$v(x, y, t) \approx \sum_{j=1}^{m} V_j(t) N_j^{(1)}(x, y) \tag{30}$$

$$w(x, y, t) \approx \sum_{j=1}^{n} \bar{\Delta}_j(t) \varphi_j(x, y) \tag{31}$$

$$\phi_x(x, y, t) \approx \sum_{j=1}^{n} \mathcal{X}_j(t) N_j^{(2)}(x, y) \tag{32}$$

$$\phi_y(x, y, t) \approx \sum_{j=1}^{n} \mathcal{Y}_j(t) N_j^{(2)}(x, y) \tag{33}$$

4 Numerical implementation

The two sets of governing equations (Eqs. 18 and 19) are solved in a staggered manner in which both the displacement and phase field are solved for alternatively. Newmark's method has been used to solve the finite element equations of the elastic equilibrium equation (18). In general, the equilibrium equation should be satisfied at any time t, i.e.

$$\left[\mathbf{K}\Delta\right]_t + \left[\mathbf{M}\ddot{\Delta}\right]_t = \mathbf{F}_t \tag{34}$$

where **K**, **M** and **F** denote the stiffness matrix, mass matrix and force vector respectively.

According to Newmark's method the time derivatives are approximated in the following manner

$$\dot{\boldsymbol{\Delta}}_{t+1} = \dot{\boldsymbol{\Delta}}_t + a_1\ddot{\boldsymbol{\Delta}}_t + a_2\ddot{\boldsymbol{\Delta}}_{t+1} \tag{35}$$

$$\boldsymbol{\Delta}_{t+1} = \boldsymbol{\Delta}_t + \dot{\boldsymbol{\Delta}}_t\Delta t + \frac{1}{2}\left[(1-\gamma)\ddot{\boldsymbol{\Delta}}_t + \gamma\ddot{\boldsymbol{\Delta}}_{t+1}\right](\Delta t)^2 \tag{36}$$

where $a_1 = (1-\alpha)\Delta t$ and $a_2 = \alpha\Delta t$, and α, γ are the Newmark's constants which control the accuracy and stability of the scheme. From Eq. (36) one can write

$$\ddot{\boldsymbol{\Delta}}_{t+1} = a_3(\boldsymbol{\Delta}_{t+1} - \boldsymbol{\Delta}_t) - a_4\dot{\boldsymbol{\Delta}}_t - a_5\ddot{\boldsymbol{\Delta}}_t \tag{37}$$

where $a_3 = \dfrac{2}{\gamma(\Delta t)^2}$, $a_4 = a_3\Delta t$, $a_5 = \dfrac{1}{\gamma} - 1$. In this work, the values of Newmark's constants α and γ are taken as 0.5, which correspond to the constant average acceleration scheme. These constants are known to give the unconditionally stable results for the linear problems. Premultiplying Eq. (37) with $\boldsymbol{M}_{t+1}$ and making use of Eq. (34), one can get the effective stiffness and force vectors as follows:

$$\hat{\boldsymbol{K}}_{t+1}\boldsymbol{\Delta}_{t+1} = \hat{\boldsymbol{F}}_{t+1} \tag{38}$$

where

$$\hat{\boldsymbol{K}}_{t+1} = \boldsymbol{K}_{t+1} + a_3\boldsymbol{M}_{t+1} \tag{39a}$$

$$\hat{\boldsymbol{F}}_{t+1} = \boldsymbol{F}_{t+1} + \boldsymbol{M}_{t+1}\left(a_3\boldsymbol{\Delta}_t + a_4\dot{\boldsymbol{\Delta}}_t + a_5\ddot{\boldsymbol{\Delta}}_t\right) \tag{39b}$$

The staggered algorithm can be described as follows

For $j = 1$ to number of time steps

(a) Freeze ϕ and solve for **u** (initialize displacements and velocities) using the elastic equilibrium equation.

(b) Calculate $\mathcal{H}^+$, then solve for ϕ using the Eq. 26

end

5 Numerical examples

In this section, numerical examples are presented to study the damage evolution in thick plates subjected to transient dynamic (uniformly distributed) load. For some of the examples presented in this section, SS-2 boundary conditions (see, Fig. 3) are considered [69]. In SS-2 boundary conditions, the following quantities are constrained. On the edges parallel to x axis, the inplane displacement along the y axis, transverse deflection and the shear deformation (rotation along y axis), N_{yy} and $\bar{M}_{yy}$ and on the edges parallel to y axis, the inplane displacement along the x axis, transverse deflection and the shear deformation (rotation along x axis), N_{xx} and $\bar{M}_{xx}$ are constrained.

Quarter plate is modeled in cases where symmetry is present and the results are assembled to see the full plate visualization. Four noded conforming rectangular finite elements are used to model the geometry of the plate. Each node of the element has 8 nodal unknowns (along with the phase field variable) as shown in Fig. 4. Selective integration scheme is used

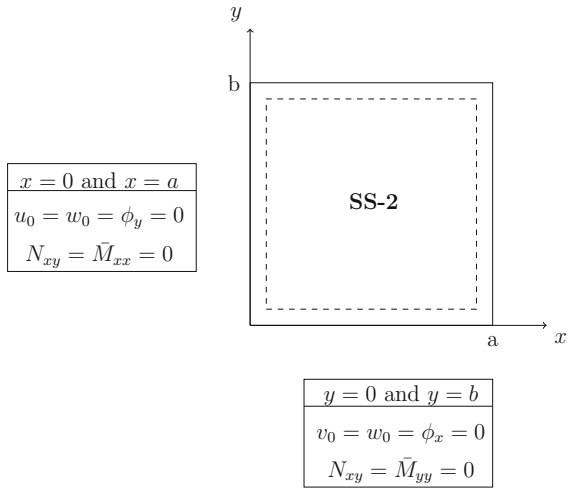

Fig. 3 SS-2 Boundary conditions

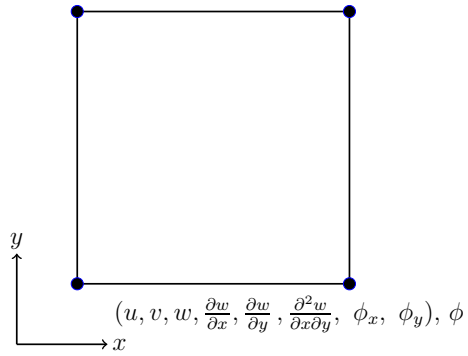

Fig. 4 Four-noded rectangular element

to evaluate the stiffness matrix. The selective integration scheme includes 2×2 Gauss rule for the bending terms and 1×1 Gauss rule for the shear and membrane terms. As it is shown in the Miehe et al. [64], the length scale parameter should be at least twice the element size to resolve the localized zone properly. This is ensured in all the examples presented. For all the examples considered, the following material properties are used:

$E = 2.1 \times 10^6$ N/cm^2, $G = 0.84 \times 10^6$ N/cm^2, - and $\rho = 8 \times 10^{-6}$Ns^2/cm^4.

5.1 Example 1: Comparison of hybrid model and No T–C model

In this example, a square plate of dimensions 25 cm $\times$ 25 cm is considered for the analysis. SS-2 boundary conditions are applied and *a*/*h* is taken as 5. Uniformly distributed (spread over the area of 0.5 cm $\times$ 0.5 cm at the center of the plate) pulse load (see Fig. 5) with $q_0 = 1800$ N/cm^2 is applied. The value of length scale parameter is taken as 0.5 cm. Number of finite elements used are 10,000.

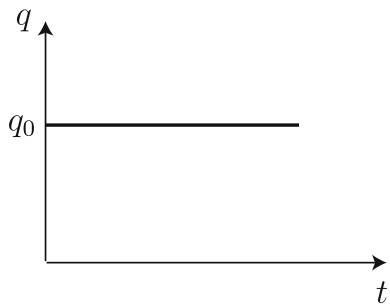

Fig. 5 Pulse load considered for the analysis

Figure 6 shows the central deflection versus time graph corresponding to hybrid model and no tension–compression (T–C) split model. As it can be seen, the two models clearly show the difference in predicting the mechanical response with time. The discrepancy is owing to the difference in the calculation of history variable. In hybrid model, the history variable is calculated based on the positive part of the strain energy where as in No T-C model, it is taken equal to the total strain energy i.e. without splitting the strain energy into tensile and compressive parts. It should also be noted that the calculation of $\mathcal{H}^+$ depends on the total strain which varies over the thickness, and not on the typical midsurface strain. Therefore, the degradation of the stiffness can vary over the thickness although the degradation function is uniform. In order to capture the shear deformation effects, TSDT has been used. This allows for the correct degradation of the positive part of the strain energy, which is essential for the prediction of damage.

Figure 7shows the deflection versus time plot with and without considering the degradation of the stiffness. In the model with no damage, the value of degradation function is taken equal to one. As expected, the model with consideration of damage predicts more deflection than the model without damage.The variation of damage at central point is plotted in Fig. 8. The irreversibility of damage is ensured by the increasing nature of $\mathcal{H}^+$ with time, therefore damage increases with time and becomes constant after reaching the value 1. The damage evolution starts from the first step of the loading itself (of course, the value of damage will be very small) and continues to grow as long as there is a driving force, which in this model is based on the history parameter $\mathcal{H}^+$. Once the material is fully damaged at a particular point (i.e. ϕ becomes 1), it remains constant at that point. Since the dissipated energy is continuously growing, and most activity of driving force is happening at the diffused interface between the phases, the interface evolves, the damage at points other than the loading foot print also keeps increasing. This explains the fact that the damage spreads, even when the material under the loading footprint is completely damaged. Figure 9 shows the differences in the damage profiles of hybrid and the No T-C model. It is seen that at a given time step, the hybrid model predicts more damage compared to the No T-C

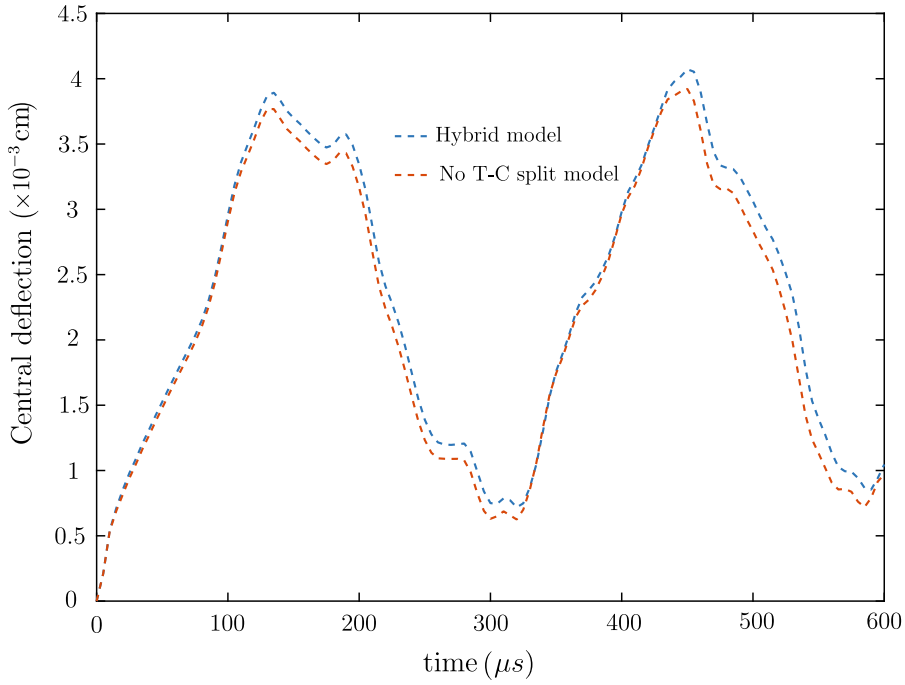

Fig. 6 Central deflection versus time graph predicted by hybrid and No T-C split models

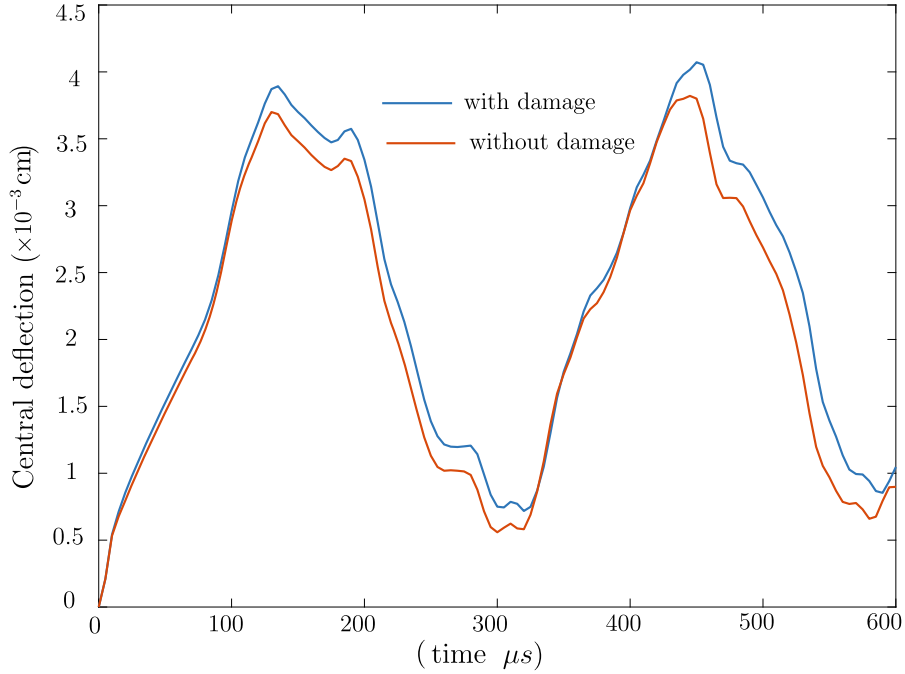

Fig. 7 Central deflection versus time with and with out considering damage

split model. Here, in the proposed approach, the calculation of history parameter i.e. $\mathcal{H}^+$ is done based on the positive part of the spectral decomposition of the tension–compression split. This in turn, depends on the total strain which varies over the thickness, and not on the typical midsurface variables. Therefore, the degradation of the stiffness can vary over the thickness although the degradation function is uniform. This

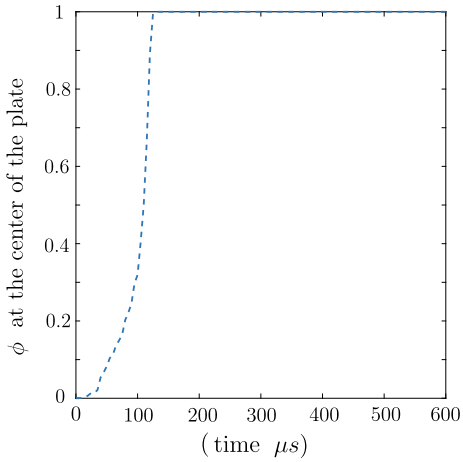

Fig. 8 Evolution of ϕ at the center of the plate

allows for the correct degradation of the positive part of the strain energy, which is essential for the prediction of damage. A similar study has been reported in literature, where in an attempt was made to consider the through thickness variation. Kiendle et al. [57] compared the damage variation through the thickness in a simply supported beam using both the solid and the KL shell elements . As it can be seen from the discussion, the solid element also predicts insignificant variation of damage through the thickness. This justifies the present simpler formulation. As the shear deformations play a significant role on the mechanical response of thick plates, third order shear deformation theory which can accurately predict the response compared to the classical and first order shear deformation theory has been used. The accurate prediction of shear strains in turn leads to correct prediction of the history parameter $\mathcal{H}^+$, which is the driving force for evolution of damage.

It should also be noted that the proposed phase field model, as is the case with the other existing models, predicts the damage from the first step of the loading itself (however, the value of damage will be very small) and continuous to grow as long as there is a driving force i.e. $\mathcal{H}^+$. In the present case the total steps are chosen by trials, when all the time steps are completed the load control loop is stopped. However, in the static analysis, one can obtain the load-displacement graph as well as the damage profile, and find the peak load the structure can carry. This will give an indicator for stopping the time steps. In case of dynamic analysis, one has to make the decision on where to stop the simulation by quantitative measurement of the damage variable. It is observed from the results that, once the material is fully damaged at a particular point (i.e. ϕ becomes 1), the value of damage remains constant at that point. Since the dissipated energy is continuously growing, and most activity of driving force is happening at the diffused interface between the phases, the interface evolves, the damage at points other than the loading foot print, also keeps increasing.

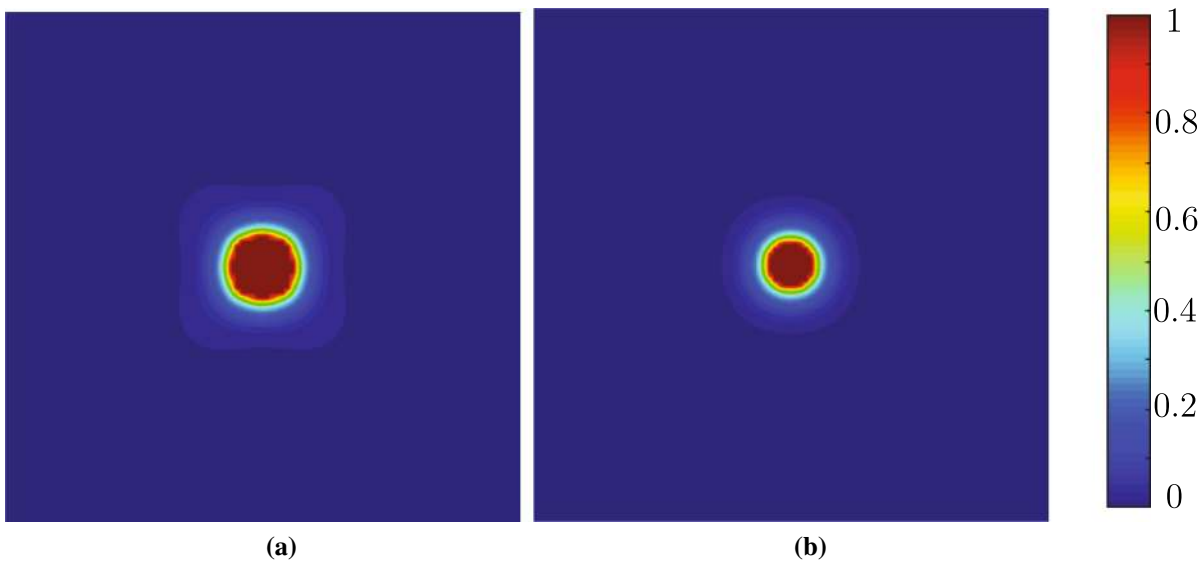

Fig. 9 Evolution of damage predicted by **a** hybrid model and **b** model with no tension–compression split at a given time step

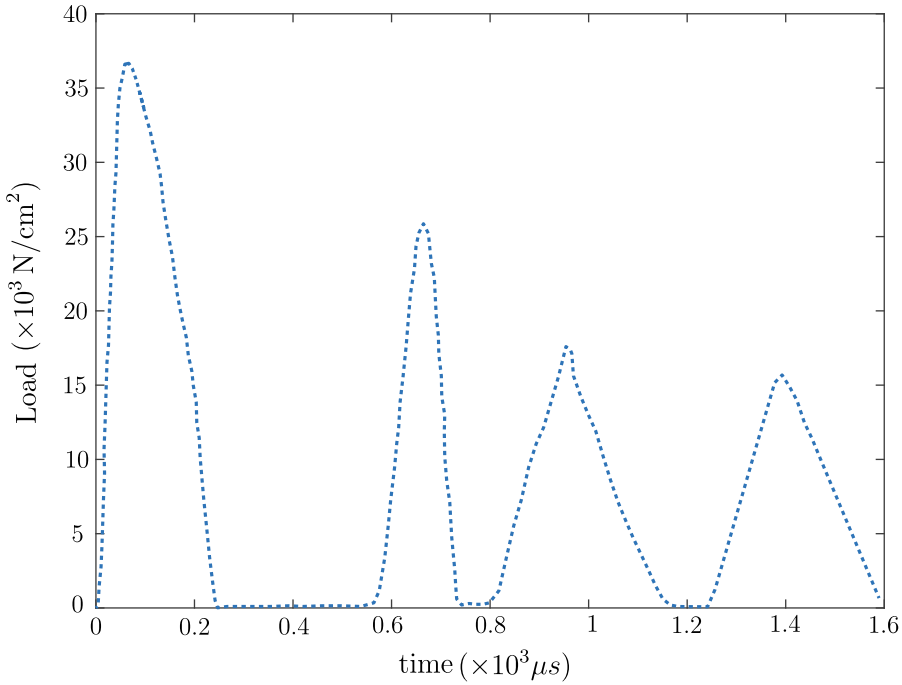

Fig. 10 Time variation of uniformly distributed load

5.2 Example 2 : Analysis of square plate

A square plate of dimensions 25 cm × 25 cm is considered for the analysis. The plate is subjected to an uniformly distributed load that varies with the time as shown in Fig. 10. The load is considered to be acting at the center of the plate (spread over the area of 0.5 cm × 0.5 cm). SS-2 boundary conditions are considered. An $a/h = 5$ is considered for the analysis. The value of length scale parameter is taken as 0.5 cm. The plate is discretized, a sufficiently refined mesh with a total number of 10,000 finite elements is considered for analysis.

Figure 11 shows the evolution of damage with the time. As it can be seen, the damage evolution starts at the center of the plate i.e. exactly under the loading footprint and propagates towards the corners of the plate as the time progresses. The damage value (ϕ) at given point remains constant after reaching the value 1. The driving force behind the evolution of damage is attributed to the available dissipated energy therefore the damage spreads in the direction in which the dissipated energy is maximum. Figure 12 shows the variation of central deflection with the time.

5.3 Example 3: Analysis of simply supported rectangular plate

A rectangular plate of dimensions 25 cm × 12.5 cm is considered for the analysis. SS-2 boundary conditions are considered. An $a/h = 5$ for the plate is considered with a being equal to 25cm. Uniformly distributed load (with time variation as shown in Fig. 10) is assumed to spread over the area of 0.5 cm × 0.25 cm at the center of the plate. The value of length scale parameter is taken as 0.5 cm. Number of finite elements used are 10,000.

Figure 13 shows the evolution of damage at different stages of time and Fig. 14 shows the variation of central deflection with time. As it can be seen, the evolution starts at the center of the plate i.e under the loading footprint and propagates towards the edges of the rectangular plate.

5.4 Example 4: Analysis of rectangular cantilever plate

In this example, a rectangular cantilever plate of dimensions 12.5 cm × 6.25 cm is considered. The value of *a/h* is taken as 5 (*a* being the length of the plate). Uniformly distributed (spread over the area of 0.25 cm × 0.25 cm) time varying load as shown in

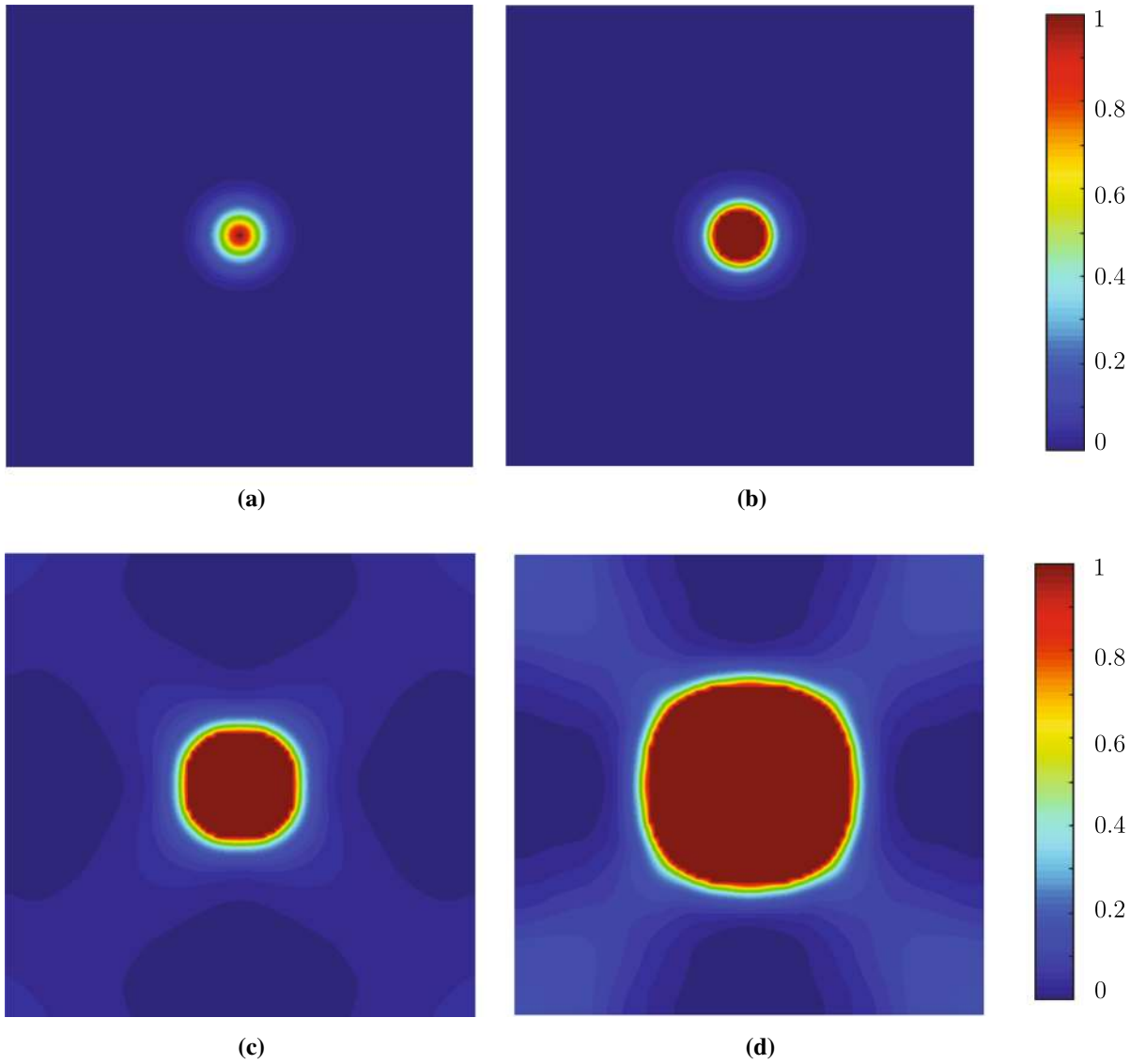

Fig. 11 Evolution of damage in a square thick plate **a–d** subjected to SS-2 boundary conditions under transient dynamic load acting at the center

Fig. 10 is considered to be acting at the center of the free edge of the cantilever of the plate. A uniform mesh of 10,000 elements is used.

Figure 15 shows the evolution of the damage. As it can be seen, the damage starts evolving at the center of the free end and gradually progresses towards the fixed end of the plate. It is also observed that the rate of increase in damage is more at the fixed end due to the more energy dissipation. Figure 16 shows the corresponding central deflection with time graph.

6 Conclusions

A new hybrid phase field model is developed to study the damage in thick plates subjected to transient

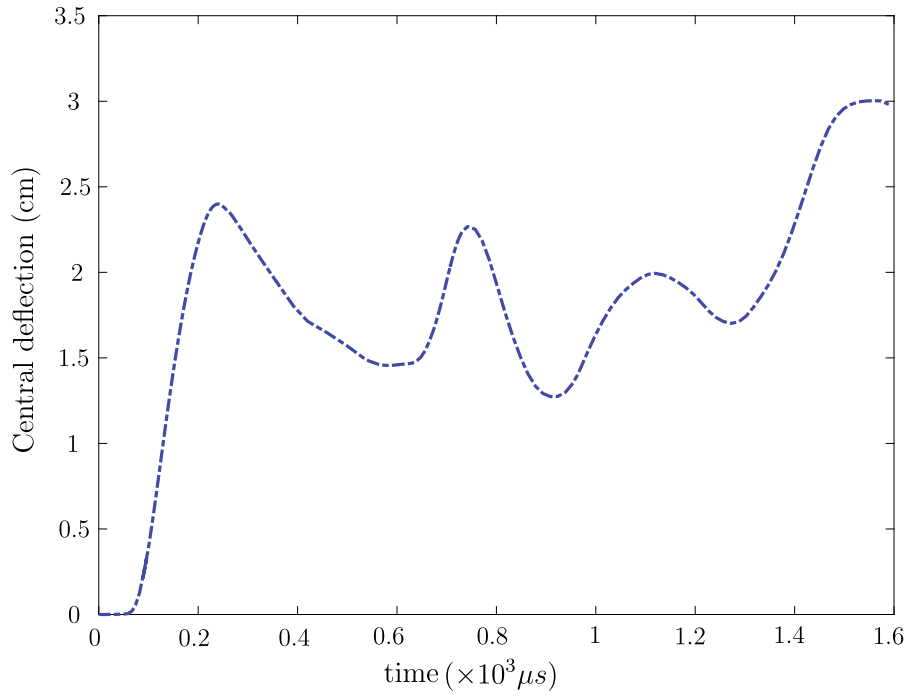

Fig. 12 Central deflection versus time graph

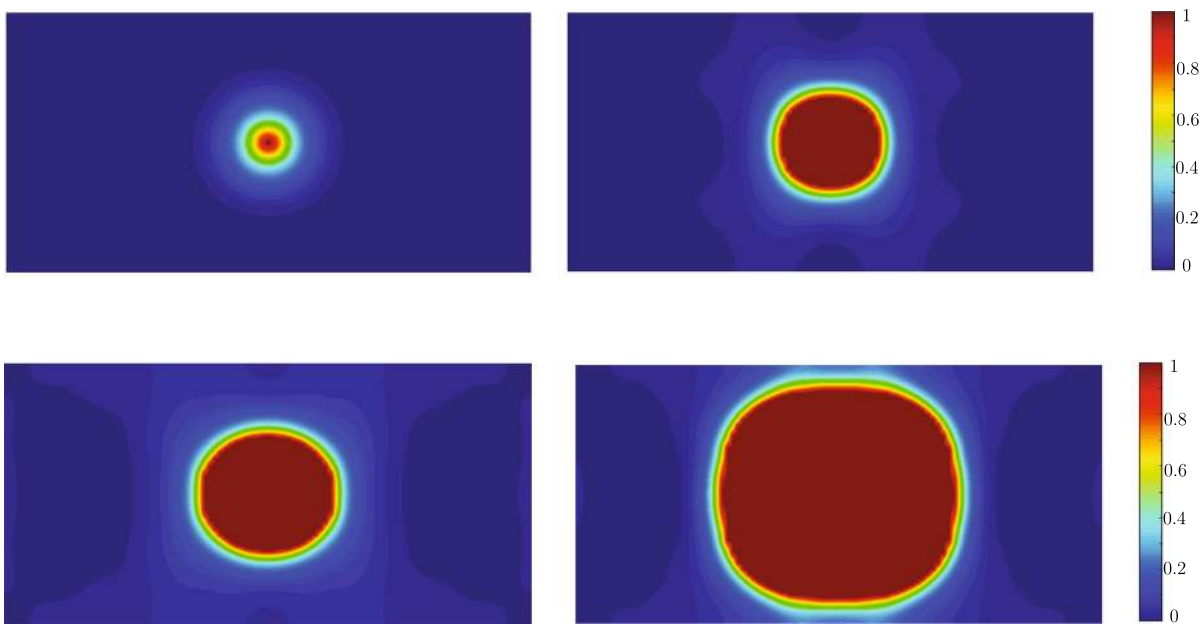

Fig. 13 Evolution of damage at different stages of loading in thin rectangular plate subjected to SS-3 boundary conditions

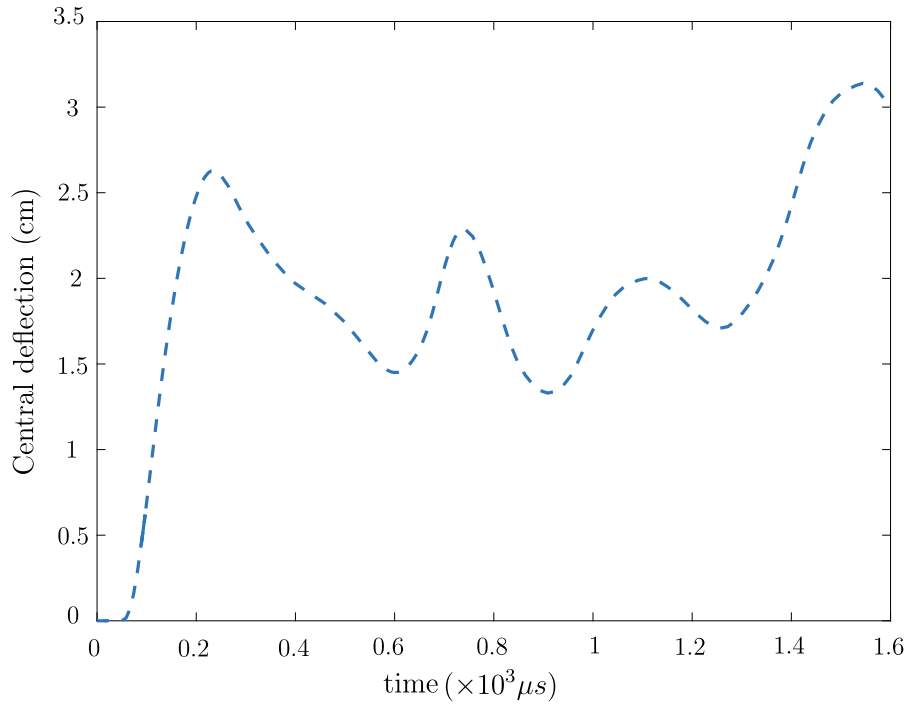

Fig. 14 Central deflection versus time graph

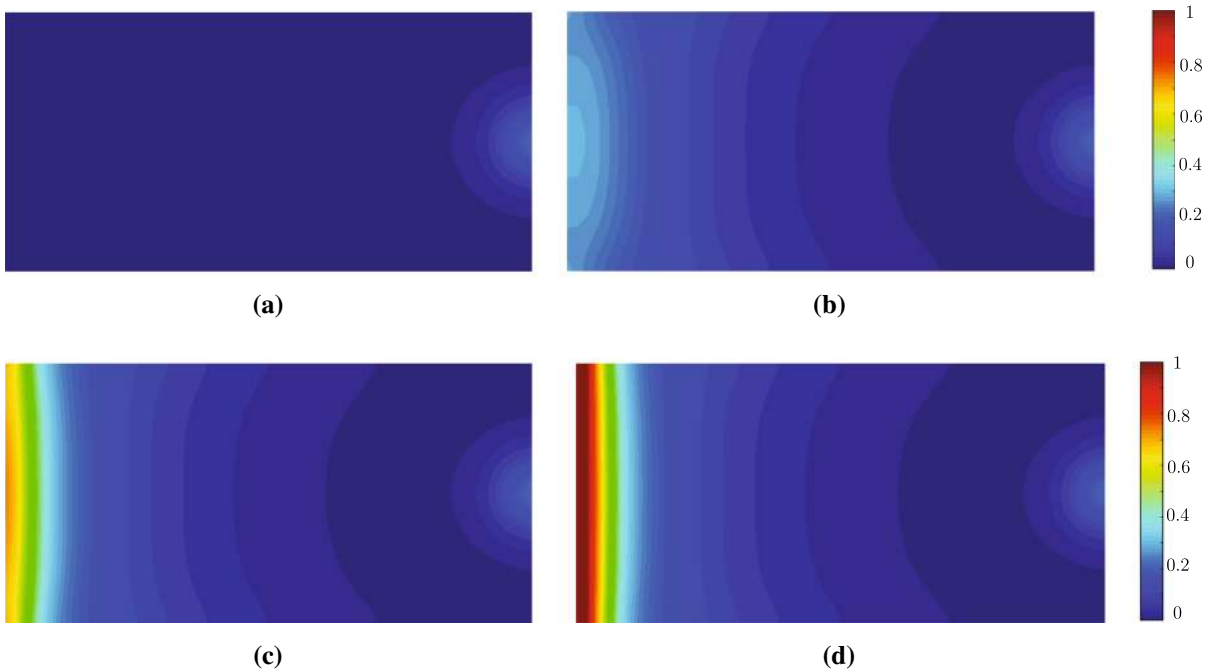

Fig. 15 Evolution of damage **a–d** at different stages of loading in thick rectangular cantilever plate

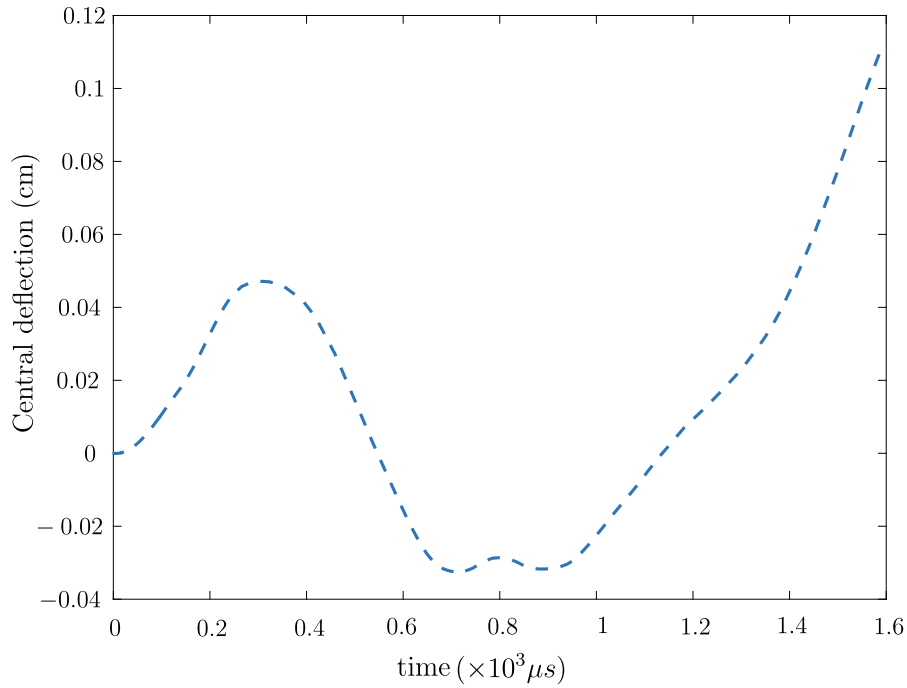

Fig. 16 Central deflection versus time graph

dynamic loads. To capture the shear deformation effects on the overall behavior, Reddy's TSDT is used. The governing equations i.e. the momentum equation and the phase field evolution equation are presented for the proposed hybrid phase field model. The governing equations are solved using a staggered solution algorithm in a finite element framework. The proposed hybrid model restores the linearity of the equations of motion with in the staggered approach and is more physically appealing as the evolution of damage is governed by the positive part of the strain energy. The proposed hybrid model and No T-C model are compared and found to be indifferent in predicting the mechanical response. Comparison between the hybrid model and the model without degrading the stiffness of the plate has also been made. The numerical examples also show the efficiency of the hybrid phase field model in finding the nucleation and propagation of damage under transient dynamic loads.

Compliance with ethical standards

Conflict of interest The authors declare that they have no conflict of interest.

References

1. Moës N, Dolbow J, Belytschko T (1999) A finite element method for crack growth without remeshing. Int J Numer Methods Eng 46(1):131–150
2. Moës N, Belytschko T (2002) Extended finite element method for cohesive crack growth. Eng Fract Mech 69(7):813–833
3. Fries TP, Belytschko T (2010) The extended/generalized finite element method: an overview of the method and its applications. Int J Numer Methods Eng 84(3):253–304
4. Xu XP, Needleman A (1994) Numerical simulations of fast crack growth in brittle solids. J Mech Phys Solids 42(9):1397–1434
5. Parmigiani JP, Thouless MD (2006) The roles of toughness and cohesive strength on crack deflection at interfaces. J Mech Phys Solids 54(2):266–287
6. de Borst R, Sluys LJ, Mühlhaus HB (1993) Fundamental issues in finite element analysis of localization of deformation. Eng Comput 10:99–121
7. Jirásek M (2004) Nonlocal theories in continuum mechanics. Acta Polytech 44:16–34
8. Pijaudier-Cabot G, Burlion N (1996) Damage and localisation in elastic materials with voids. Int J Mech Cohes Frict Mater 1:129–144
9. Bažant ZP, Pijaudier-Cabot G (1988) Nonlocal continuum damage, localization instability and convergence. J Appl Mech 55:521–539
10. Peerlings RHJ, de Borst R, Brekelmans WAM (1996) Gradient-enhanced damage for quasi-brittle materials. Int J Numer Meth Eng 39(39):3391–3403
11. Giry C, Dufour F, Mazars J (2011) Stress based nonlocal damage model. Int J Solids Struct 48(25–26):3431–3443

12. Lorentz E (2017) A nonlocal damage model for plain concrete consistent with cohesive fracture. Int J Fract 207:123–159
13. Francfort GA, Marigo JJ (1998) Revisiting brittle fracture as an energy minimization problem. J Mech Phys Solids 46:1319–1342
14. Griffith AA (1921) The phenomena of rupture and flow in solids. Philos Trans R Soc Lond Ser A 221:163–198
15. Bourdin B, Francfort GA, Marigo JJ (2000) Numerical experiments in revisited brittle fracture. J Mech Phys Solids 48:797–826
16. Ambrosio L, Tortorelli VM (1990) Approximation of functional depending on jumps by elliptic functional via t-convergence. Commun Pure Appl Math 43(8):999–1036
17. Raina A, Miehe C (2016) A phase-field model for fracture in biological tissues. Biomech Model Mechanobiol 15:479–496
18. Borden MJ, Hughes TJR, Landis CM, Anvari A, Lee IJ (2016) A phase-field formulation for fracture in ductile materials: finite deformation balance law derivation, plastic degradation, and stress triaxiality effects. Comput Methods Appl Mech Eng 312:130–166
19. Lee S, Wheeler MF, Wick T (2016) Pressure and fluid-driven fracture propagation in porous media using an adaptive finite element phase field model. Comput Methods Appl Mech Eng 305:111–132
20. Teichtmeister S, Kienle D, Aldakheel F, Keip MA (2017) Phase field modelling of fracture in anisotropic brittle solids. Int J Non-linear Mech 97:1–21
21. Pham KH, Ravi-Chandar K, Landis CM (2017) Experimental validation of a phase field model for fracture. Int J Fract 205:83–101
22. Alessi R, Ambati M, Gerasimov T, Vidoli S, De Lorenzis L (2018) Comparison of phase-field models of fracture coupled with plasticity. Adv Comput Plast 46:1–21
23. Tanné E, Li T, Bourdin B, Marigo JJ, Maurini C (2018) Crack nucleation in variational phase field models of brittle fracture. J Mech Phys Solids 110:80–99
24. Areias P, Reinoso J, Camanho PP, César de Sá J, Rabczuk T (2018) Effective 2D and 3D crack propagation with local mesh refinement and the screened Poisson equation. Eng Fract Mech 189:339–360
25. Msekh MA, Cuong NH, Zi G, Areias P, Zhuang X, Rabczuk T (2018) Fracture properties prediction of clay/epoxy nano composites with interphase zones using a phase field model. Eng Fract Mech 188:287–299
26. Ambati M, Gerasimov T, De Lorenzis L (2015) A review on phase-field models of brittle fracture and a new fast hybrid formulation. Comput Mech 55(2):383–405
27. Ambati M, De Lorenzis L (2016) Phase-field modeling of brittle and ductile fracture in shells with isogeometric NURBS-based solid-shell elements. Comput Methods Appl Mech Eng 312:351–373
28. Miehe C, Teichtmeister S, Aldakheel F (2016) Phase-field modelling of ductile fracture: a variational gradient-extended plasticity-damage theory and its micromorphic regularization. Philos Trans R Soc A 374:1–18
29. Rodriguez P, Ulloa J, Samaniego C, Samaniego E (2018) A variational approach to the phase field modeling of brittle and ductile fracture. Int J Mech Sci 144:502–517
30. Aldakheel F, Hudobivnik B, Wriggers P (2019) Virtual element formulation for phase-field modeling of ductile fracture. Int J Multiscale Comput Eng 17(2):181–200
31. Areias P, Rabczuk T (2013) Finite strain fracture of plates and shells with configurational forces and edge rotations. Int J Numer Meth Eng 94:1099–1122
32. Ambati M, Kruse R, De Lorenzis L (2016) A phase-field model for ductile fracture at finite strains and its experimental verification. Comput Mech 57(1):149–167
33. Aldakheel F, Wriggers P, Miehe C (2018) A modified Gurson-type plasticity model at finite strains: formulation, numerical analysis and phase-field coupling. Comput Mech 62:815–833
34. Singh N, Verhoosel CV, van Brummelen EH (2018) Finite element simulation of pressure-loaded phase-field fractures. Meccanica 53:1513–1545
35. Bilgen C, Kopaničáková A, Krause R, Weinberg K (2018) A phase-field approach to conchoidal fracture. Meccanica 53:1203–1219
36. Borden MJ, Hughes TJR, Landis CM, Verhoosel CV (2014) A higher-order phase-field model for brittle fracture: formulation and analysis within the isogeometric analysis framework. Comput Methods Appl Mech Eng 273:100–118
37. Kasirajan P, Bhattacharya S, Rajagopal A, Reddy JN (2020) Phase field modeling of fracture in quasi-brittle materials using natural neighbor galerkin method. Phase field modeling of fracture in Quasi-Brittle materials using natural neighbor Galerkin method 366:113019
38. Verhoosel CV, de Borst R (2013) A phase-field model for cohesive fracture. Int J Numer Meth Eng 96:43–62
39. Vignollet J, May S, de Borst R, Verhoosel CV (2014) Phase field models for brittle and cohesive fracture. Meccanica 49:2587–2601
40. Alessi R, Marigo JJ, Vidoli S (2014) Gradient damage models coupled with plasticity and nucleation of cohesive cracks. Arch Ration Mech Anal 214(2):575–615
41. Paggi M, Reinoso J (2017) Revisiting the problem of a crack impinging on an interface: a modeling framework for the interaction between the phase field approach for brittle fracture and the interface cohesive zone model. Comput Methods Appl Mech Eng 321:145–172
42. Zhang P, Hu X, Wang X, Yao W (2018) An iteration scheme for phase field model for cohesive fracture and its implementation in Abaqus. Comput Mech 204:268–287
43. Geelen RJM, Liu Y, Hu T, Tupek MR, Dolbow JE (2019) A phase-field formulation for dynamic cohesive fracture. Mech Mater 348:680–711
44. Hansen-Dörr AC, De Borst R, Hennig P, Kästner M (2019) Phase-field modelling of interface failure in brittle materials. Comput Methods Appl Mech Eng 346:25–42
45. Reinoso J, Arteiro A, Paggi M, Camanho PP (2017) Strength prediction of notched thin ply laminates using finite fracture mechanics and the phase field approach. Compos Sci Technol 150:205–216
46. B. Dhas, MD. Masiur Rahaman, K. Akella, D. Roy, and J.N. Reddy. A phase field damage model for orthotropic materials and delamination in composites. *Journal of Applied Mechanics*, 85(1):1–11, 2017
47. Bleyer J, Alessi R (2018) Phase-field modeling of anisotropic brittle fracture including several damage mechanisms. Comput Methods Appl Mech Eng 336:213–236

48. Carollo V, Reinoso J, Paggi M (2018) Modeling complex crack paths in ceramic laminates: a novel variational framework combining the phase field method of fracture and the cohesive zone model. J Eur Ceram Soc 38:2994–3003
49. Solmaz T, John L, Axel V, Steven W (2009) A new phase-field model for strongly anisotropic systems. Proc R Soc A 465:1337–1359
50. Rajagopal A, Fischer P, Kuhl E, Steinmann P (2010) Natural element analysis of the Cahn–Hilliard phase field model. Comput Mech 46:471–493
51. Bin L, Christian P, Daniel M, Irene A, Marino A (2014) Phase-field modeling and simulation of fracture in brittle materials with strongly anisotropic surface energy. Int J Numer Meth Eng 102(3–4):711–727
52. Karma A, Kessler DA, Levine H (2001) Phase-field model of mode III dynamic fracture. Phys Rev Lett 87(4)
53. Hofacker M, Miehe C (2013) A phase field model of dynamic fracture: Robust field updates for the analysis of complex crack patterns. Int J Numer Meth Eng 93(3):276–301
54. Borden MJ, Verhoosel CV, Scott MA, Hughes TJR, Landis CM (2012) A phase-field description of dynamic brittle fracture. Comput Methods Appl Mech Eng 217–220:77–95
55. Nguyen VP, Wu JY (2018) Modeling dynamic fracture of solids with a phase-field regularized cohesive zone model. Comput Methods Appl Mech Eng 340:1000–1022
56. Amiri F, Millán D, Shen Y, Rabczuk T, Arroyo M (2014) Phase field modelling of fracture in linear thin shells. Theoret Appl Fract Mech 69:102–109
57. Kiendl J, Ambati M, De Lorenzis L, Gomez H, Reali A (2016) Phase-field description of brittle fracture in plates and shells. Comput Methods Appl Mech Eng 312:374–394
58. Raghu P, Rajagopal A, Reddy JN (2020) Thermodynamically consistent variational approach for modeling brittle fracture in thick plates by a hybrid phase field model. ASME J Appl Mech 87(2):021002
59. Areias P, Rabczuk T, Msekh MA (2016) Phase-field analysis of finite strain plates and shells including element subdivision. Comput Methods Appl Mech Eng 312:322–350
60. Lai W, Gao J, Li Y, Arroyo M, Shen Y (2020) Phase-field modeling of brittle fracture in Euler-Bernoulli beam accounting for transverse part-through thickness. Comput Methods Appl Mech Eng 361:112787
61. Reddy JN (1984) A simple higher-order theory for laminated plates. J Appl Mech 51:745–752
62. Amor H, Marigo JJ, Maurini C (2009) Regularized formulation of the variational brittle fracture with unilateral contact: numerical experiments. J Mech Phys Solids 57:1209–1229
63. Miehe C, Hofacker M, Welschinger F (2010) A phase field model for rate-independent crack propagation: robust algorithmic implementation based on operator splits. Comput Methods Appl Mech Eng 199:2765–2778
64. Miehe C, Welschinger F, Hofacker M (2010b) Thermodynamically consistent phase-field models of fracture: Variational principles and multi-field FE implementations. Int J Numer Meth Eng 83:1273–1311
65. Wu JY (2018) Robust numerical implementation of non-standard phase-field damage models for failure in solids. Comput Methods Appl Mech Eng 340:767–797
66. Raghu P, Rajagopal A, Reddy JN (2018) Nonlocal nonlinear finite element analysis of composite plates using TSDT. Compos Struct 185:38–50
67. Raghu P, Rajagopal A, Reddy JN (2020) Nonlocal transient dynamic analysis of laminated composite plates. Mech Adv Mater Struct 27(13):1076–1084
68. Srividhya S, Raghu P, Rajagopal A, Reddy JN (2018) Nonlocal nonlinear analysis of functionally graded plates using third-order shear deformation theory. Int J Eng Sci 125:1–22
69. Reddy JN (2007) Theory and analysis of elastic plates and shells. CRC Press, Cleveland